PNAS RESEARCH ARTICLE | ENGINEERING

# Self-sacrificing and self-supporting biomass carbon anode–assisted water electrolysis for low-cost hydrogen production

Yuming Huang[a], Wei Zhou[a,1], Liang Xie[a], Xiaoxiao Meng[a], Junfeng Li[a], Jihui Gao[a], Guangbo Zhao[a], and Yukun Qin[a]

Affiliations are included on p. 10.

Edited by Alexis Bell, University of California, Berkeley, CA; received September 20, 2023; accepted September 4, 2024

**Electrooxidation of renewable and $CO_2$-neutral biomass for low-cost hydrogen production is a promising and green technology. Various biomass platform molecules (BPMs) oxidation assisted hydrogen production technologies have obtained noticeable progress. However, BPMs anodic oxidation is highly dependent on electrocatalysts, and the oxidation mechanism is ambiguous. Meanwhile, the complexity and insolubility of natural biomass severely constrain the efficient utilization of biomass resources. Here, we develop a self-sacrificing and self-supporting carbon anode (SSCA) using waste corncobs. The combined results from multiple characterizations reveal that the structure-property-activity relationship of SSCA in carbon oxidation reaction (COR). Theoretical calculations demonstrate that carbon atoms with a high spin density play a pivotal role in reducing the adsorption energy of the reactive oxygen intermediate (*OH) during the transition from $OH^-$ to *OH, thereby promoting COR. Additionally, the HER||COR system allows driving a current density of 400 $mAcm_{geo}^{-2}$ at 1.24 V at 80 °C, with a hydrogen production electric consumption of 2.96 kWh $Nm^{-3}$ ($H_2$). The strategy provides a ground-breaking perspective on the large-scale utilization of biomass and low-energy water electrolysis for hydrogen production.**

hydrogen production | biomass | carbon anode | carbon oxidation reaction

## Significance

In comparison to water electrolysis, the electrolysis of biomass feedstock to generate $H_2$requires much lower theoretical electricity consumption, but current technologies struggle to directly utilize water-insoluble biomass. The preparation cost of soluble biomass platform molecules (BPMs) and catalysts will undoubtedly increase the total cost of biomass electrolysis for hydrogen production. Instead of continuously exploring new electrocatalysts with complex architectures to reduce the overpotential of the partially soluble BPMs oxidation reactions, the focus is diverted to other innovative strategies. The development of metal-free catalysts and the direct use of biomass for electrolysis to produce hydrogen might be the ultimate path toward industrialization with a reduced economic burden.

Hydrogen, as a clean, high-energy density, renewable energy source, is expected to replace fossil energy and solve the energy crisis and environmental problems (1). Electrocatalytic water splitting using renewable energy (e.g., solar energy, wind) has been recognized as an efficient and prospective sustainable technology to gain hydrogen (2). The sluggish four-electron transfer and high overpotential of oxygen evolution reaction (OER), however, is the main bottleneck limiting the high efficiency of water electrolysis (WE) (3). Although considerable efforts have been devoted to designing high-performance OER electrocatalysts, more than 90% of the input energy still needs to be consumed to drive WE (4). Based on the above, the development of novel anodic oxidation reactions with more favorable kinetics and thermodynamics than OER is a feasible approach to fundamentally reduce the energy requirements for WE (Fig. 1, *Left*) (5). To date, two primary classes of substances suitable for integration with electrochemical hydrogen production have been extensively reported. One category is organic small molecules, such as lower and aromatic alcohols (1), primary or benzyl amines (6, 7), and biomass platform molecules (BPMs) (8, 9). The other category is waste resources, such as ammonia (10), urea (11), hydrazine hydrate (12), waste PET plastics (13), and chitin (14). Among them, approximately 100 billion tons of biomass waste generated globally each year have already resulted in the waste of biomass energy (15). Accordingly, the utilization of waste biomass for energy-saving hydrogen production by electro-oxidation technology will have broad prospects in terms of ecology, energy, and economy.

Over the past 5 y, there has been significant progress in biomass-assisted WE (BAWE) for hydrogen production, but addressing the following challenges remains a challenging endeavor. For instance, from economic perspective, the real economic worth of the majority of biomass by-products resulting from BAWE is often lower than the total value of the consumed feedstocks. Moreover, these biomass feedstocks exhibit limited yields and come with high costs, susceptible to market fluctuations. In the long run, the viability of this technology hinges on the availability of substantial raw material reserves and markets for the generated by-products (16). Additionally, biomass electrochemical oxidation reaction (BEOR) is highly dependent on electrocatalysts (17). Among them, noble metal catalysts still dominate the catalytic processes of various BPMs (4). Unfortunately, these catalysts are often expensive, complex to synthesize, and prone to poisoning by in situ generated intermediates (e.g., CO), limiting their feasibility for large-scale applications (18). To date,

Author contributions: Y.H., W.Z., and X.M. designed research; Y.H. and W.Z. performed research; L.X. and G.Z. contributed new reagents/analytic tools; Y.H., W.Z., J.L., J.G., and Y.Q. analyzed data; X.M. funding acquisition; J.L. discussion and methodology; J.G. supervision and writing—review & editing; G.Z. and Y.Q. writing—review & editing; and Y.H. and W.Z. wrote the paper.

The authors declare no competing interest.

This article is a PNAS Direct Submission.

[1] To whom correspondence may be addressed. Email: hitzhouw@hit.edu.cn.

This article contains supporting information online at https://www.pnas.org/lookup/suppl/doi:10.1073/pnas.2316352121/-/DCSupplemental.

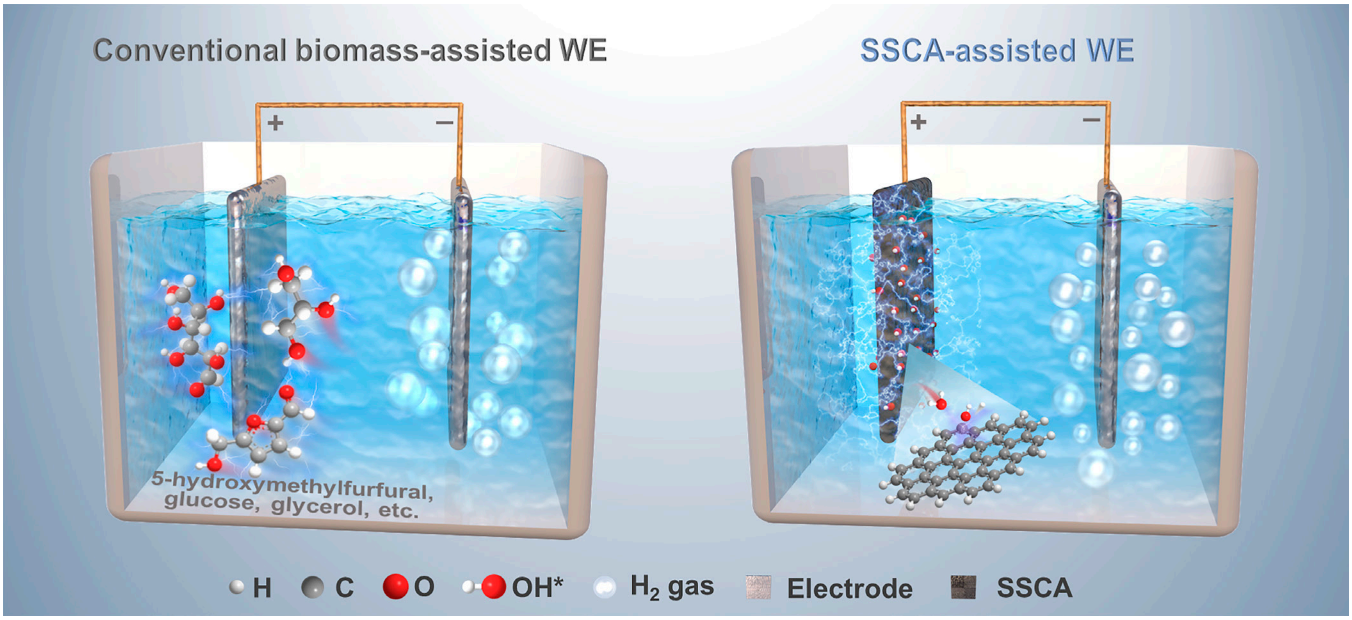

**Fig. 1.** Schematic diagram of conventional BPMs assisted WE (*Left*) and SSCA assisted WE for hydrogen production (*Right*).

some nonnoble metal catalysts, owing to their competitive pricing, reduced poisoning effects, and enhanced catalytic activity in biomass oxidation, have garnered increased interest. There remains, however, much controversy regarding the origin of the activity of nonnoble metal electrocatalysts in BEOR (7, 19–21). In addition, external factors such as the reaction temperature, reactant concentration, type of electrolyte, could also affect the catalytic activity of electrocatalysts (16, 22–24). Besides, the solubility of biomass feedstocks is also a tricky issue. Current research on BEOR is limited to soluble BPMs, given that the conventional WE system is a pure aqueous solution system. There are few reports on natural biomass or solid carbon in nonpure aqueous solution system (*SI Appendix*, Fig. S1) to assist WE for hydrogen production (25–29). Insoluble carbon sources introduce mass transfer challenges that critically impede catalytic conversion efficiency of the anode, rendering high current density hydrogen production at low voltages unattainable (30). In light of this, rather than persistently investigating new electrocatalysts with intricate architectures to decrease overpotential in partially soluble biomass oxidation reactions, attention is redirected toward innovative strategies aimed at designing more universally applicable, efficient, and cost-effective BAWE technologies.

Carbon, renowned for its exceptional conductivity, is extensively as part of the electrode in electrocatalysis and battery applications (31). Nonetheless, the vulnerability of carbon to corrosion is a notable challenge, and researchers have devoted significant efforts to developing carbon materials with enhanced corrosion stability to suppress carbon oxidation (31–33). We noticed that there is often a neglect of in-depth exploration of the carbon oxidation reaction (COR) mechanism and the development of COR-utilizing technologies. Here, we propose a concept in the WE that maximally utilizes COR in the carbon electrode to replace OER for assisting WE. In detail, a unique BAWE system (Fig. 1, *Right*) coupling hydrogen evolution reaction (HER) with COR of a self-sacrificing and self-supporting carbon anode (SSCA) is designed to solve the above challenges in non-OER WE. This integrated carbon anode is prepared from waste corncob biomass which has the possibility for massive production. The evolution of carbon structures in COR is investigated via transmission electron microscopy (TEM), scanning electron microscopy (SEM), electron paramagnetic resonance (EPR), and in situ Raman spectroscopy. The COR mechanism is identified by operando electrochemical impedance spectroscopy (EIS), ex situ EPR, and rotating ring-disk electrode (RRDE). Combining experiments and density functional theory calculations, we propose that the electrocatalytic oxidation of carbon mainly involves reactive oxygen intermediates (ROIs), *OH, *O, and *OOH, generated by electron transfer of OH$^-$. As those carbon atoms possessing unpaired electrons have a very low *OH adsorption free energy, the carbon anode can generate *OH in situ and be oxidized by *OH in situ. Benefitting from the direct electron transfer (DET) pathway of electron transfer from OH$^-$ to the carbon anode. The SSCA exhibits superior electro-oxidation performance, delivering an oxidation current density of 50 mAcm$_{geo}^{-2}$ at 1.48 V vs. RHE. In addition, the HER||COR system, composed of LHBC-10-2.6 electrodes, achieves an industrial-level current density (400 mAcm$_{geo}^{-2}$) at only 1.24 V at 80 °C, with a hydrogen production electric consumption of 2.96 kWh Nm$^{-3}$ (H$_2$). This work provides a profoundly effective strategy for combining large-scale biomass utilization with low-energy consumption hydrogen production to facilitate the energy transition to a zero-carbon economy.

## Results and Discussion

**Materials Characterizations.** Multiple material characterization instruments were utilized to investigate the structural properties of SSCAs. The morphology and structures of HBC samples were presented in SEM and TEM images. From the SEM images (*SI Appendix*, Figs. S2 and S3), all samples show a spherical morphology formed by aggregation of spherical nanoparticles, while the only difference is the apparent formation of new layered structures on the surface for the carbon spheres of HBC-9 and HBC-10. The layered structure is produced via polycondensation of aromatic carbon and cross-linking between the free radicals (34). And the layered structure is majorly formed in the temperature range of 900 to 1,000 °C as condensation energies of aromatic rings are approximately 400 to 470 kJ/mol (35). The HRTEM image,

Fig. 2*A*, reveals that the HBC sample is composed of amorphous carbon structure with no discernible crystal lattice fringes. Upon annealing of the HBC sample at 1,000 °C, it exhibits a similar onion-like carbon structure (Fig. 2*B*). The inner core of the onion-like carbon structure consists of amorphous carbon (Fig. 2*C*) and is surrounded by graphitic carbon (Fig. 2*D*). Notably, observable vacancy defects (red dotted circle marks) in the long-range graphite network strongly suggest the possible existence of dangling bonds within HBC-10. These dangling bonds at the base and edges of the onion-like carbon usually represent those carbon atoms containing unpaired electrons (36). HRTEM images of HBC samples were further analyzed for binarization and edge extraction using Photoshop and QIA-64 software, respectively (*SI Appendix*, Fig. S4). Fringe lengths <0.3 nm (i.e., invalid noise) were eliminated. As depicted in Fig. 2*E* and *SI Appendix*, Table S2, the mean and median values of lattice fringes of HBC samples exhibited an overall increasing trend with the rise in annealing temperature. As can be seen from XRD patterns in *SI Appendix*, Fig. S5, HBC-6 to HBC-10 samples exhibit two broad diffraction peaks at around 24° and 42°, corresponding to the (002) and (100) planes of graphitic carbon (37).

As favorable electrical conductivity of the carbon anode is the prerequisite for COR to take place. The resistivity of HBC samples was measured by a four-point probe resistivity meter, which in turn assessed the conductivity of HBC samples. Fig. 2*F* displays a positive correlation between the conductivity of HBC samples and the annealing temperature. The size of graphite microcrystals in carbon anodes increases with higher annealing temperatures, promoting favorable conditions for electron transfer and reducing the resistivity of the carbon anode. Notably, the self-supporting carbon anode exhibits a substantially higher conductivity (0.8 S $m^{-1}$ at 1 MPa) compared to the powder form (0.0152 S $m^{-1}$ at 1 MPa), resulting in a notable improvement in the efficiency of electron transfer from carbon to the circuit. Raman spectroscopy of HBC samples is shown in Fig. 2*G*, and two prominent characteristic peaks at 1,340 $cm^{-1}$ (D band, defective graphitic structure) and 1,590 $cm^{-1}$ (G band, crystalline graphite) are observed in the Raman spectra (38, 39). Similar $I_D/I_G$ values across all samples

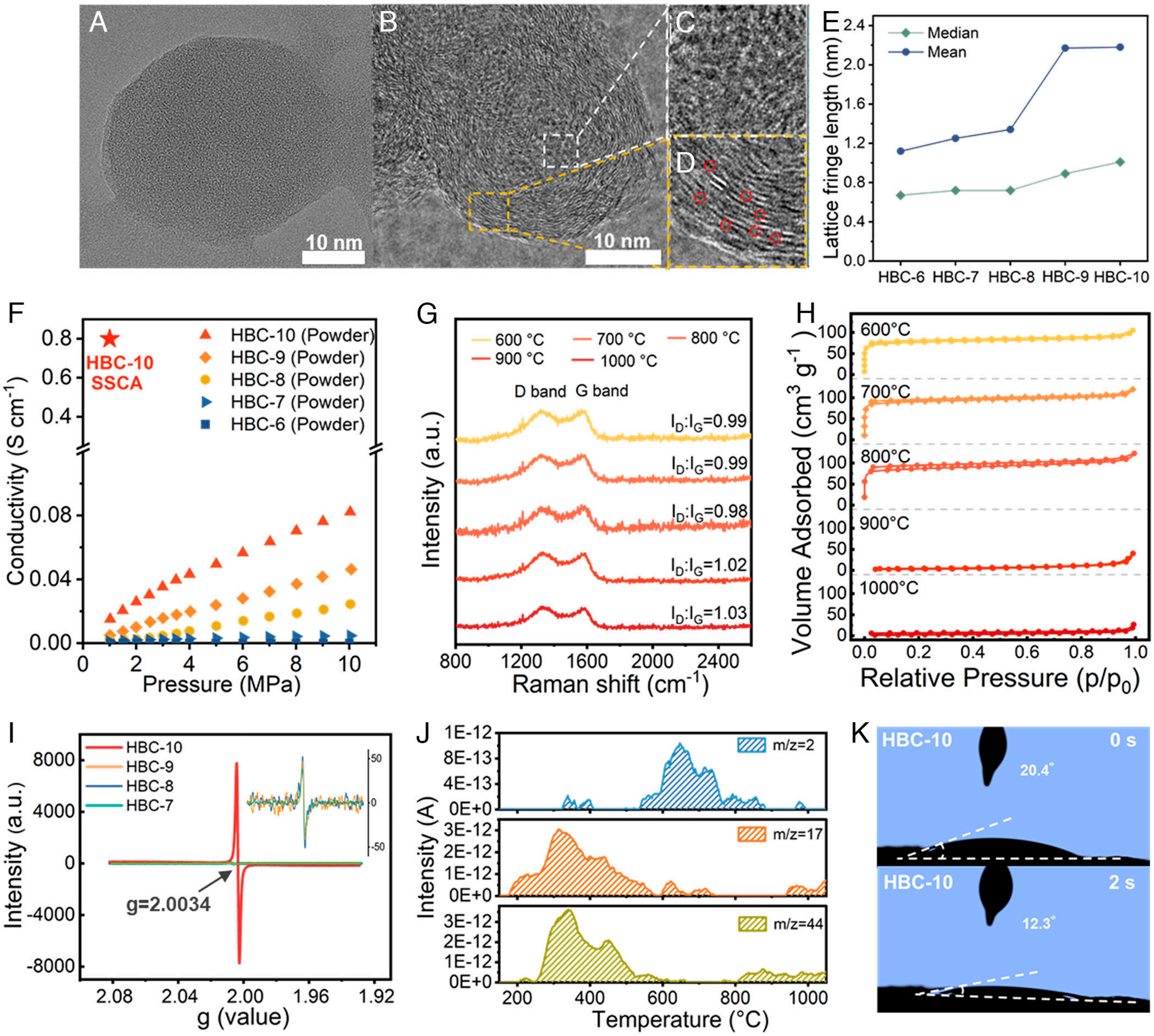

**Fig. 2.** Material characterization of SSCAs. HRTEM images of (*A*) HBC and (*B*) HBC-10; (*C*) the *C* is corresponding to the area of white dotted box of *B*; (*D*) the *D* is corresponding to the area of yellow dotted box of *B*; (*E*) lattice fringe length from HRTEM fringe data of HBC samples; (*F*) electric conductivity, (*G*) Raman spectra, (*H*) $N_2$ adsorption/desorption isotherms, and (*I*) EPR spectra of HBC samples; (*J*) In situ thermogravimetry-mass spectrum test (MS signal of m/z = 2, 17, 44) of HBC; (*K*) the contact angles of HBC-10.

suggest a comparable content of amorphous carbon and graphite carbon structures in HBC samples. Combined with HRTEM analysis, the carbon structure of HBC-10 is more probably to construct "Order-in-Disorder" engineering, where the long-range graphite network surrounds the carbon defect region in situ. The influence of annealing temperature on the pore structure of HBC samples was investigated by nitrogen adsorption (Fig. 2*H*). From *SI Appendix*, Table S3, it can be found that the specific surface area of HBC samples first increased with higher annealing temperature, in the following order: HBC (9.16 $m^2$ $g^{-1}$) <HBC-6 (237.06 $m^2$ $g^{-1}$) <HBC-7 (277.54 $m^2$ $g^{-1}$), and then the opposite trend was shown that the specific surface area of the HBC-9 (88.49 $m^2$ $g^{-1}$) and HBC-10 (7.74 $m^2$ $g^{-1}$) samples rapidly decreased compared to HBC-8 (265.48 $m^2$ $g^{-1}$). Besides, the pore volume of micropores and mesopores in HBC samples decreased with increasing temperature when the pyrolysis temperature was higher than 700 °C (*SI Appendix*, Fig. S6). The annealing process has a considerable effect on the surface structure of HBC. When the pyrolysis temperature rises high enough, "thermal deactivation" effect becomes dominant, resulting in char melting, structural ordering, and pore fuse (40).

The annealing process of biomass could induce the homolytic cleavage of covalent bonds to form atoms or groups with unpaired electrons, called persistent free radicals (PFRs) (41). The information about unpaired electrons in the prepared HBC-X was acquired by EPR spectroscopy at room temperature as shown in Fig. 2*I* and *SI Appendix*, Fig. S7. All samples present a single Lorentzian line with a *g* value of 2.0034, which is associated with unpaired electrons of $sp^2$-carbon atoms within π-conjugated aromatic rings (42, 43). HBC-6 has the strongest EPR signal, and the next is HBC-10, whose signal intensity is about 160 times higher than that of HBC-7, HBC-8, and HBC-9. The EPR results imply that a great number of PFRs are present in HBC-6 and HBC-10 samples. The evolution mechanism of PFRs for HBC sample was explored by TG-MS analysis from room temperature to 1,000 °C under argon atmosphere. The corresponding TG curve is presented in *SI Appendix*, Fig. S8 and in situ thermogravimetry-mass spectra are shown in Fig. 2*J* and *SI Appendix*, Fig. S9. The TG curve confirmed that the mass decline process of HBC mainly occurred before 600 °C, as most of oxygen groups of carbon backbones were removed, companying PFRs formed simultaneously (44, 45). This could explain why there are tremendous radicals can be experimentally found in HBC-6. However, the PFRs formed after the pyrolysis of functional groups have high activity and may be reoxidized or evolved into new surface structures subsequently (44). Therefore, the PFRs content of the samples annealed at 700 °C to 900 °C decreases rapidly. Upon increasing the annealing temperature to 1,000 °C, those stable functional groups, such as C–H, marginal C–O–C, and C=O, are removed in the carbon skeleton and the new surface structure (*SI Appendix*, Fig. S10) (46, 47). Therefore, a lot of PFRs are regenerated in HBC-10. Besides, in comparison to other samples (*SI Appendix*, Fig. S11), the surface of HBC-10 is more hydrophilic with the smallest contact angle of 20.4° (12.3° after 2 s), which facilitates mass transfer and surface reaction processes (Fig. 2*K*). Apparently, the high curvature of the nanosphere structure on the surface of HBC-10 is covered by a two-dimensional carbon layer due to the thermal deactivation effect, and the reduction of surface roughness results in a relatively favorable wettability of HBC-10.

**Electrochemical Analysis of COR.** During the electro-oxidation of carbon, the water oxidation reactions (WORs) and COR may both occur at SSCA. In Fig. 3*A*, all SSCA samples exhibit two oxidation stages, COR I and COR II, except the HBC-6 with low oxidation activity due to its lower electrical conductivity (Detailed information for SSCA samples shown in *SI Appendix*, Table S4). COR I is typically the oxidation of the disordered domains and molecularly functionalized carbon structures, such as phenanthrene (PE), phenanthrenecarboxylic acid (PCA), and xanthene (X) structures (33, 48). However, the intrinsic low conductivity of these carbon structures prevents achieving higher currents for COR I. COR II (>1.2 V vs. RHE) involves the catalytic oxidation stage related to water. The EIS data of HBC-7 to HBC-10 were fitted by the optimal fitting model in *SI Appendix*, Fig. S12, and the EIS data of HBC-6 were fitted by the model in the *Upper Right Inset* of *SI Appendix*, Fig. S13. The $R_1$ and $R_2$ represent the resistance of COR I (internal oxidation of the carbon electrode) and COR II (oxidation at the electrolyte–carbon interface), respectively. As seen in the EIS fitting results (*SI Appendix*, Table S5), HBC-10 has the lowest resistance for both COR I ($R_1$ = 0.436 Ω) and COR II ($R_2$ = 1.558 Ω), suggesting that HBC-10 has faster charge transfer kinetics for COR I and COR II at 1.8 V *vs.* RHE. The HBC-10 shows a higher oxidation performance $(50\ \mathrm{mAcm}_{\mathrm{geo}}^{-2}\ @\ 1.48\ \mathrm{V})$ compared with other samples. The same conclusion was obtained when the mass activity (A $g^{-1}$, *SI Appendix*, Fig. S14) and specific activity ($\mathrm{mAcm}_{\mathrm{catalyst}}^{-2}$, *SI Appendix*, Fig. S15) was used as an evaluation guideline. And the oxidative performance of the HBC-10 is even superior to the commercial $RuO_2$. According to a linear relationship between Δj/2 (1.10 V) and the scan rate (*SI Appendix*, Fig. S16), the calculated electrochemical active area (ESCA) of HBC-10 is 110.34 $cm^2$, surpassing other samples and the $Ru_2O$ catalyst (49.15 $cm^2$), as shown in *SI Appendix*, Table S6. The dissolution phenomenon of carbon anodes is related to the oxidation time and the oxidation potential. The larger the oxidation potential of the carbon anode in the same time, the more mass it loses (*SI Appendix*, Fig. S17 and Table S7). To analyze the catalytic kinetics of electrochemical oxidation for HBC-10, the Operando EIS was employed to monitor the changes in the reaction interface of the electrode at various potentials. The corresponding Bode phase plots of HBC-10, as illustrated in Fig. 3*B*, present two electrochemical processes, which are associated with interface reaction charge transfer in the low frequency region and the electro-oxidation of the electrode in the high frequency region, respectively (49, 50). The high-frequency region ($10^1$ to $10^5$ Hz) was generally regarded as oxidation of the electrode inner. The low-frequency ($10^{-1}$ to $10^1$ Hz) region is considered to be associated with the interface oxidation, which is related to the nonhomogeneous charge distribution caused by surface oxidized species (9, 50). In the range of 0.4 to 1.8 V vs. RHE, a peak presented in the low frequency region indicates that the first-stage oxidation reaction is caused by the oxidation of some carbon structures in the carbon anode (51). When the potential increases to about 1.6 V vs. RHE, there is a semicircle begins to take shape in the high frequency region, which indicates that $OH^-$ begins to be oxidized on the carbon anode surface ($OH^- \rightarrow {}^*OH + e^-$) (8).

Accurate identification of WORs on the surface of the carbon anode is essential. The RRDE technique was employed to confirm whether the second-stage oxidation process of HBC-10 included WORs (two-electron or four-electron) (52). Fig. 3*C* shows that no oxygen reduction reaction (ORR) currents are detected at the Pt ring electrode either in COR I or in COR II, indicating that $OH^-$ ions are not anodized to $O_2$ by HBC-10. Also, $H_2O_2$ is not detected during the oxidation of HBC-10 when the ring potential is 1.465 V vs. RHE using RRDE measurements (*SI Appendix*, Fig. S18). Subsequently, we examined the potential gas products

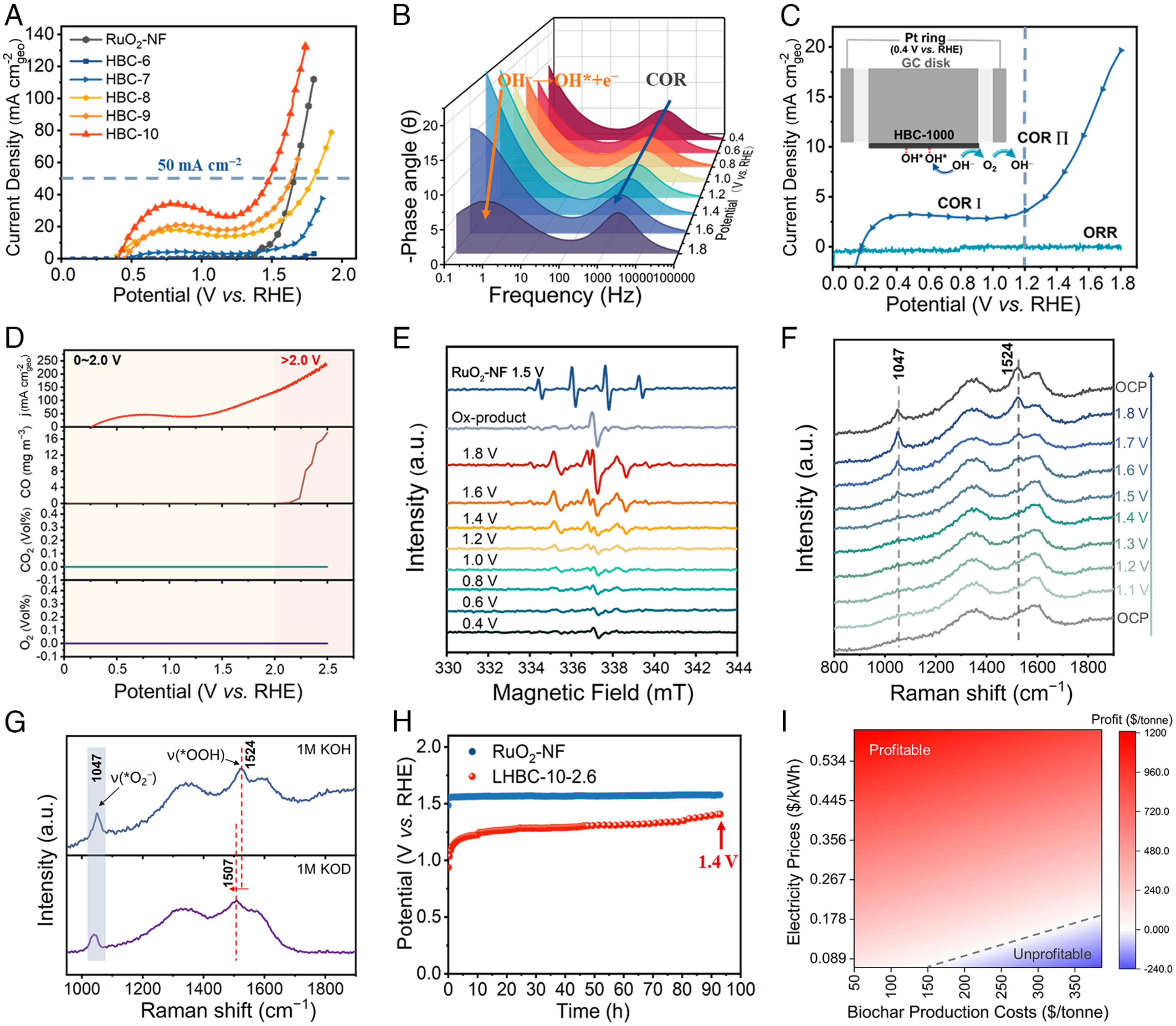

**Fig. 3.** Investigations of COR performance and mechanism for SSCA. (*A*) LSV curves for HBC samples and RuO$_2$-NF in 1 M KOH (90%-iR compensation was applied, and all currents were normalized to the projected geometric area of anode, respectively); (*B*) Operando Bode phase plots of HBC-10 at various potentials in 1 M KOH; (*C*) Detection of O$_2$ evolution from the HBC-10 using RRDE measurements (*Inset* shows the schematic of RRDE detection). The potential at the Pt ring is set at 0.4 V vs. RHE to reduce the oxygen generated during the anodic polarization scan; (*D*) different gas product concentration curves at various potentials of HBC-10 (without iR compensation); (*E*) ex situ EPR spectra of solutions after HBC-10 oxidated at different potentials in 1 M KOH with 0.1 M DMPO; (*F*) in situ EC-SERS of HBC-10 in 1 M KOH at different potentials; (*G*) in situ EC-SERS of HBC-10 in 1 M KOH (*Upper* panel) and 1 M KOD (*Lower* panel); (*H*) chronoamperometry (20 mA) curve for LHBC-10 and RuO$_2$-NF, respectively; (*I*) profitability analysis for biochar assisted WE for hydrogen production technology.

of HBC-10 during COR over a broader range of potentials. As shown in Fig. 3*D*, CO, CO$_2$, and O$_2$ were not detected directly in the range of 0 to 2.0 V vs. RHE for COR, however, the concentration of CO starts to increase gradually when the potential was higher than 2.0 V vs. RHE. At 2.5 V vs. RHE, the CO concentration reached 17.58 mg cm$^{-3}$, and still no CO$_2$ and O$_2$ gas products were detected. Since CO$_2$ could dissolve and form carbonates in high pH electrolytes (53), we first carried out a constant potential test of HBC-10 at 1.6 V vs. RHE for 3 h (*SI Appendix*, Fig. S19*A*), and then the electrolyte was acidified by rapidly injecting 5 M H$_2$SO$_4$ to completely shift the CO$_2$/CO$_3^{2-}$ balance to CO$_2$. It can be seen that there is still no CO$_2$ product after acidification of the electrolyte (*SI Appendix*, Fig. S19*B*). Nevertheless, when we applied a potential of HBC-10 at 2.5 V vs. RHE for 3 h (*SI Appendix*, Fig. S20), the mass of HBC-10 decreased from 0.1127 g to 0.0407 g, with a carbon loss of 0.072 g. Among the losing carbon, 2.58% was converted to CO (6.024 mg), 40.83% was converted to CO$_2$ (107.8 mg), and 56.59% of the carbon dissolved in the electrolyte.

The evolution of ROIs and the dynamic surface structure of HBC-10 during the COR II process were investigated using ex situ EPR and in situ electrochemical surface-enhanced Raman spectroscopy (EC-SERS). 5,5-dimethylpyrroline-N-oxide (DMPO) was added to the electrolyte as a spin-trapping agent for these ROIs (*OH and *OOH), and the EPR signals of HBC-10 after operating at different potentials for 3 min was recorded (54). No EPR signals of DMPO-·OH adduct are detected when the HBC-10 is subjected to an applied potential of 0.4 to 1.8 V vs. RHE (Fig. 3*E*). Unlike the EPR results on the RuO$_2$-NF electrode, the HBC-10 exhibits no evidence of generating intermediate species (*OH) from WOR (one-electron). The HBC-10 also fails to generate the final product of WOR (one-electron) due to the applied potential range (0.4 to 1.8 V vs. RHE) being below the standard electrode potential of ·OH formation (2.38 V vs. RHE). The ex situ EPR results seem to conflict with the in situ EIS results, but the fact is that the EPR tests could not directly reflect whether or not electron transfer occurs during the reaction. One possible reason is that *OH can react with most unsaturated molecules in HBC-10 at reaction rates close to diffusion. The resulting adsorbed *OH can rapidly form "C~*OH" on carbon surface, and once they are covalently bound to carbon, any *OH will be unable to react with other oxidizable substrates or desorb and form ·OH (aq) (55). Meanwhile, a new triplet EPR signal characteristic belonging to the oxidized DMPO radical appeared, since DMPO can be oxidized at high potentials (54). Interestingly, a strong Lorentz peak with g value of 2.003 was detected in the electrolyte, when we applied a potential of 1.8 V vs. RHE to the HBC-10 in electrolyte without DMPO. The signal of this characteristic peak is derived from the product of carbon anodization exfoliation (ox-product), indicating that there may be a homolytic reaction of covalent bonds during the carbon anodization exfoliation process.

The in situ EC-SERS of HBC-10 are shown in Fig. 3*F*, and peaks at 1,047 $cm^{-1}$ and 1,524 $cm^{-1}$ appear and intensify significantly as the potential rises to approximately 1.6 V vs. RHE and above, indicating that the two Raman vibrational peaks may be associated with intermediates generated during the WOR processes. Furthermore, when the potential is switched back to open-circuit potential, the Raman peaks at 1,047 $cm^{-1}$ and 1,524 $cm^{-1}$ do not disappear, suggesting that ROIs could stably exist on the carbon surface rich in free radicals and are difficult to desorb. To precisely identify ROIs during the COR process, deuterium (D) isotope substitution experiments were conducted. D isotope substitution experiments (Fig. 3 *G*, *Lower* panel) revealed that the peak at 1,524 $cm^{-1}$ shifted to a lower wavenumber at 1,507 $cm^{-1}$, indicating that ROIs containing H are adsorbed. Quantitative calculations based on chemical shifts further attribute this peak to the O–O vibration in *OOH. The Raman peak at 1,047 $cm^{-1}$, typically associated with $*O_2^-$ (*OOH deprotonates to form $*O_2^-$), showed no peak shift in H/D isotopic substitution experiments (Fig. 3*G*), confirming the absence of H in this intermediate (56). In the COR II process for HBC-10, gas analysis experiments showed no $O_2$ generation, but SERS detected the presence of ROIs, suggesting that COR II could generate ROIs which cannot desorb from the HBC-10 surface. Therefore, the carbon anode may undergo structural changes due to oxidation by ROIs (*OH, *O, and *OOH) during the catalytic water oxidation process. Combined with the in situ Bode plots analysis, the second oxidation stage of HBC-10 could attribute that $OH^-$ is catalyzed by HBC-10 to form ROIs. Afterward, these ROIs might be rapidly utilized to oxidize HBC-10 and be converted to oxygen functional group (hydroxyl and carbonyl groups), so there are no other ROIs available for WORs.

The COR process induces irreversible changes in the carbon structure, thereby shortening the operating lifespan of the carbon anode under low potential conditions. Generally, mechanical replacement of anodes and increasing the mass of carbon anodes can be adopted to maintain the low energy operation of the WE system. Hence, we adopted a larger mold (3 cm × 6 cm, *SI Appendix*, Fig. S21) to prepare a larger mass of SSCA, labeled LHBC-10-2.6, to obtain a higher oxidation current, as shown in the inset in *SI Appendix*, Fig. S22. The oxidation efficiency of the self-supporting LHBC-10-2.6 (310 mA@1.4 V) far exceeds that of 2.6 g of powdered HBC-10 (using a 3 × 6 cm $RuO_2/IrO_2/Ti$ anode) with an oxidation efficiency of 9 mA@1.4 V. Furthermore, as depicted in Fig. 3*H* and *SI Appendix*, Fig. S23, the duration for the oxidation potential to reach 1.4 V vs. RHE extends from 0.5 h to 93 h with an increase in the mass of the carbon anode from 0.112 g to 2.680 g. During the constant current oxidation period, LHBC-10-2.6 transferred a total charge of 6,646 C, while the electrode mass decreased from 2.680 g to 2.439 g. The charge transferred by COR I is only 370.8 C, while the charge transferred by COR II is 6,325.2 C, which is 94.5 % of the total charge of COR (*SI Appendix*, Fig. S24). In the electro-oxidation process of carbon, COR II takes on a more crucial role. The enhanced oxidation activity of the self-supporting carbon structure is attributed to that SSCA effectively addresses two mass transfer issues in conventional CAWE. Primarily, it shortens the path for carbon particles to reach the anode. Additionally, it significantly reduces the electron transfer resistance from carbon to the circuit. We further performed a break-even analysis of the production cost per ton of biochar (including raw biomass cost, transport cost, and pyrolysis cost) versus the benefit from the hydrogen production electricity saved by consuming per ton of biochar (calculation methods in supplementary information), as shown in Fig. 3*I*. Without considering the benefits from other value-added products generated by the SSCA-assisted WE technology, the lower the biochar production cost (<150 $/ton), the greater the benefit from the saved hydrogen production energy consumption.

**Evolution of Carbon Structure in COR.** For a more in-depth understanding of the structure–activity relationship between material structure and performance, in situ and ex situ evolution of carbon structure during COR were investigated. For the convenience of description, the LHBC-10-2.6 after the chronoamperometry test was labeled as HBCC-10. According to XPS spectra, the concentration of O atoms in HBCC-10 significantly increased from 9.7 at% to 27.7 at%, indicating profound oxidation of carbon by $OH^-$. In this context, O increases mainly in the form of C–O bond (from hydroxyl at 286.2 eV) and O=C–O (from carboxyl, esters at 289.2 eV) (57, 58), as shown in Fig. 4*A* and *SI Appendix*, Table S8. Meanwhile, the signal intensity of the PFR characteristic peak in HBCC-10 shows a significant decline when compared with HBC-10 (Figs. 2*D* and 4*B*), which again demonstrated that the concentration of PFRs was closely related to COR activity. Additionally, the features of the carbon structure for HBC-10 were examined in more detail using HRTEM. In contrast to HBC-6 (*SI Appendix*, Fig. S25), the graphite microcrystal size of HBC-10 is larger, and constitutes nano-graphite conductive networks that provide a fast electron transport path around the amorphous carbon (COR I) and the carbon radical (COR II). Therefore, the relatively higher carbon radical content and intrinsic conductivity enable HBC-10 to have the highest COR performance. As the annealing temperature continued to increase, the intrinsic conductivity of HBC-11 and HBC-12 also continued to increase (*SI Appendix*, Table S9), however, the carbon radical concentration decreased (*SI Appendix*, Fig. S26). As a result, HBC-11 and HBC-12 had lower electrocatalytic oxidation activities than HBC-10, but both were higher than HBC-6 (*SI Appendix*, Fig. S27). In conclusion, the critical factor for achieving high COR performance lies in the regulation of the annealing temperature, which governs the delicate balance between the concentration of carbon radicals and the inherent electrical conductivity within the carbon anode (*SI Appendix*, Fig. S28).

Subsequently we carried out in situ Raman spectroscopy to visualize the structural changes of the HBC-10 carbon anode during the electro-oxidation process. As indicated in Fig. 4*D*, the $I_D/I_G$ values of HBC-10 display a trend of slowly increasing and then dramatically decreasing. These two trends alternate as the carbon is continuously oxidized. For instance, the $I_D/I_G$ value first increased from the initial 1.03 to 1.28 (3rd min), followed by a

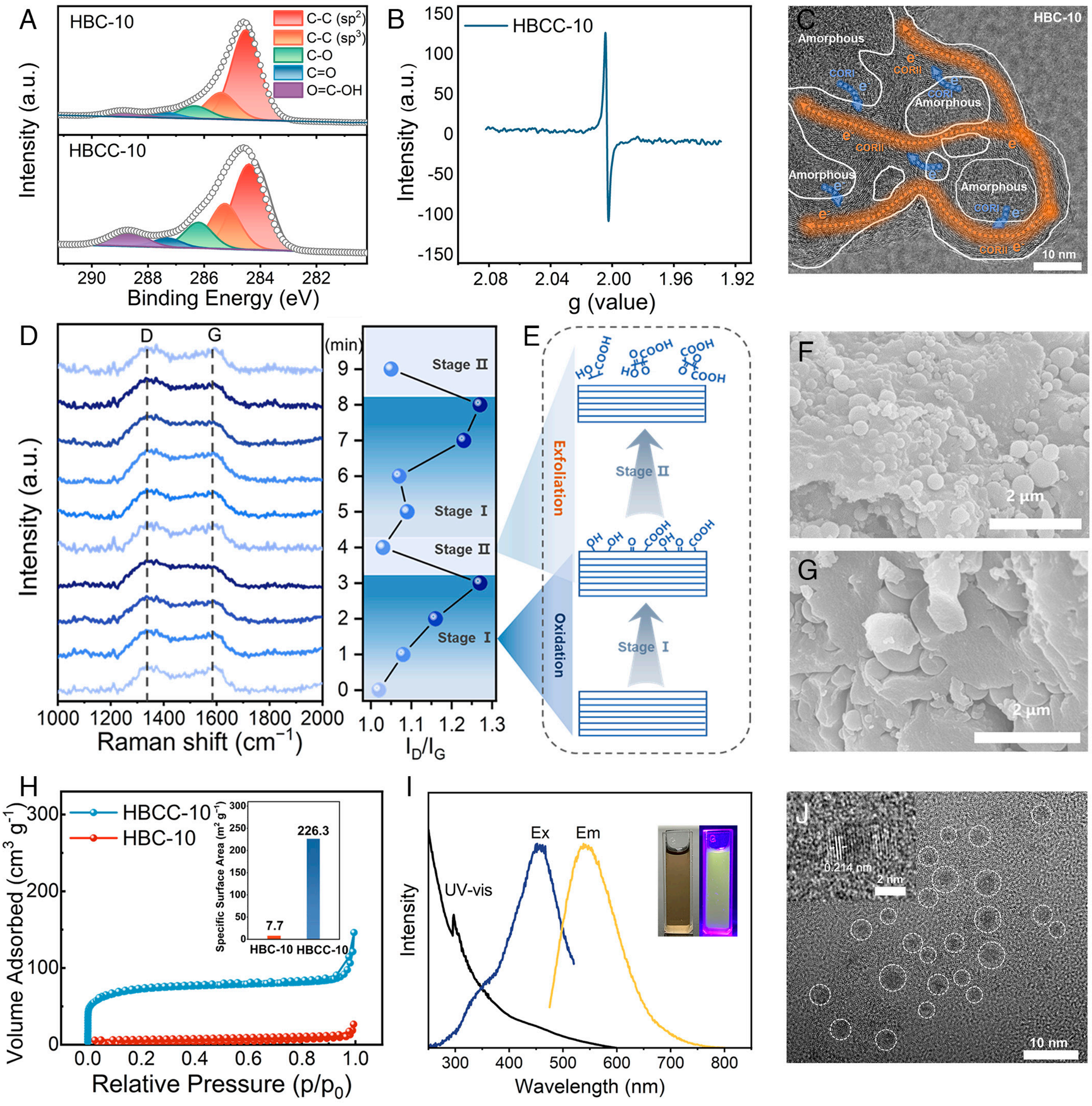

**Fig. 4.** Evolution of carbon structure in COR. (*A*) Deconvoluted C 1s spectra of HBC-10 and HBCC-10; (*B*) EPR spectra of HBCC-10; (*C*) HRTEM image for graphite microcrystalline structure of HBC-10 (blue arrows represent COR I and yellow arrows represent COR II); (*D*) in situ Raman spectra of HBC-10 in 1 M KOH at 1.4 V vs. RHE; (*E*) schematic diagram of the electro-oxidation process of carbon; SEM images of (*F*) HBCC-10 and (*G*) HBC-10; (*H*) $N_2$ adsorption/desorption isotherms of HBC-10 and HBCC-10. The *Inset* is the calculated specific surface area of HBC-10 and HBCC-10; (*I*) UV–Vis, PL emission, and PL excitation spectra of CDs exfoliated from LHBC-10-2.6. The *Inset* shows photographs of the CDs solution under daylight (*Left*) and UV light at 254 nm (*Right*); (*J*) TEM image of CDs exfoliated from LHBC-10-2.6 (*Insets*: corresponding HRTEM image).

sudden decrease to 1.04 (4th min). According to the variation regularity of HBC-10 $I_D/I_G$ and the ex situ EPR analysis, the evolution of carbon structures during electro-oxidation can be summarized in two stages. First, as illustrated in Fig. 4*E*, the oxidation stage: the carbon anode surface is oxidized by the adsorbed *OH to yield hydroxyl groups, which continue to be oxidized to higher-order oxygen functional groups. Second, the exfoliation stage: the carbon layer may undergo covalent bond breaking as well as become more hydrophilic during the oxidation. In case the outermost carbon layer induces an $I_D/I_G$ value greater than 1.28 due to electrochemical oxidation, the carbon layer is more inclined to undergo an exfoliation process while a fresh carbon layer with a lower $I_D/I_G$ value will be exposed. The morphological changes of carbon could also corroborate the electro-oxidation process of carbon described above. From the SEM images of HBCC-10 (Fig. 4*F*) and HBC-10 (Fig. 4*G*), the carbon layer covering the surface of the carbon sphere disappears. And, the specific surface area of HBCC-10 increased to 226.3 $m^2\ g^{-1}$, which is 29 times higher than before oxidation (*Inset* in Fig. 4*H*).

These exfoliated carbon layers exhibit a solubility of <0.642 g/100 g 1 M KOH at 25 °C and their optical properties were investigated by ultraviolet–visible (UV–Vis) absorption and photoluminescence (PL) spectroscopy. As shown in Fig. 4*I*, the UV–Vis spectrum of these exfoliated carbon layers exhibits an absorption peak around

297 nm, which is due to the $\pi \rightarrow \pi^*$ transition of the aromatic C=C bond (59). Additionally, the maximum PL excitation and emission wavelengths of exfoliated carbon layers are 455 nm and 540 nm, respectively. The microstructures of exfoliated carbon layers were also investigated using TEM. It can be seen from the *Inset* of Fig. 4*J*, exfoliated carbon layers display an average lattice spacing of about 0.214 nm, corresponding to the (100) crystal plane of graphitic carbon. The chemical and physical properties of these exfoliated carbon layers are similar to those of carbon dots (CDs). Therefore, these exfoliated hydrophilic CDs in solution are a more valuable carbon nanomaterial with applications in electrochemical energy storage, electrocatalysis, sensors, drug delivery, and other fields (60). The liquid phase products of HBC-10 after electrooxidation were also identified by GC-MS as seen in *SI Appendix*, Fig. S29 and Table S10. There were mostly alkanes, olefins, carboxylic acids, and alcohols with carbon numbers ranging from $C_2$ to $C_{18}$ in the liquid phase products, which could be employed as a raw material for organic synthesis, pharmaceuticals, chemicals, and fuels.

**DFT Calculations and SSCA-Assisted WE.** The self-sacrificial electrocatalytic oxidation mechanism of carbon (COR II), playing a more important role in COR process, is further revealed by DFT calculations. The electrocatalytic oxidation performance of COR II is found to be strongly related to dangling bonds (unpaired electrons on π-conjugated carbon atoms) located on the nano-graphite network, as observed through surface characterization techniques. And considering the actual lattice fringes size from the HRTEM image of HBC-10 and the stability of the computational model (*SI Appendix*, Figs. S30 and S31), a carbon cluster (M1, *SI Appendix*, Fig. S32*A*), consisting of 14 benzene rings with an unpaired electron was adopted as a model for the DFT calculations. The spin density contour maps of the carbon cluster model were plotted (*SI Appendix*, Fig. S32*B*), and it is evident that the spin density on the carbon atom ($C_{45}$) is greater. After calculating $\Delta E_{(*OH)}$ for each carbon atom in the carbon cluster model, a negative correlation was found between $\Delta E_{(*OH)}$ and the spin population, i.e., carbon atoms possessing small spin population value have a tendency to give a higher adsorption energy for *OH. And Fig. 5*A* shows that the $C_{45}$ atom with the largest spin population value (0.9) has the minimum *OH adsorption energy (–2.2 eV) compared to that of other carbon atoms, suggesting a strong interaction between the *OH and $C_{45.}$ At the same time, the stronger $\Delta E_{(*OH)}$ renders the dissociation of *OH from such carbon atoms almost impossible and may hinder the subsequent OER process.

Next, the COR and WORs free energy diagrams triggered by water were calculated to explore the excellent activity of HBC-10 and the pivotal role of PFRs in the electrocatalytic oxidation of carbon. As presented in Fig. 5*B*, the thermodynamic tendency of a $OH^-$ ion to lose an electron and generate *OH catalyzed by unpaired electron carbon atoms is remarkably low. As for COR, C ~ *OH undergoes a proton–electron transfer process to C=O at a certain potential. After that, $OH^-$ could proceed to lose an electron to generate *OH by the catalytic oxidation of C=O. The fourth basic reaction to produce *OH on the adjacent carbon is the RDS (1.41 eV). And then, a spontaneous ring opening reaction occurs between the two carbon atoms which are converted to C=O and O=C–OH, respectively. Finally, the oxygen functional groups (C=O, O=C–OH) on the oxidized carbon cluster (M6) may be thermodynamically spontaneously converted to CO/$CO_2$ (–0.40 eV, –1.06 eV). Therefore, if the oxidized carbon layer is not immediately exfoliated into the electrolyte, it may be further oxidized to CO or $CO_2$. In addition, as displayed in *SI Appendix*, Figs. S33 and S34, other possible COR routes (COR R2, COR R3, and COR R4) were calculated, and the free energy change of the RDS for other COR routes is 2.14 eV (COR R2), 1.54 eV (COR R3), and 1.54 eV (COR R4), respectively. For the possible WORs, the RDS free energy changes are 4.57 eV (one-electron), 5.42 eV (two-electron), and 3.69 eV (four-electron), respectively, which are all higher than those of the possible COR routes. We as well obtained the activation energies of HBC-10 at different potentials from the LSV curves of HBC-10 at different temperatures (calculation methods in *SI Appendix*). A comparison of the COR activation energies obtained experimentally with the COR and WORs activation energies from theoretical calculations is presented in Fig. 5*C*. The calculated activation energy barriers for COR routes (COR R1, COR R3, and COR R4) are all lower than those measured experimentally when the applied potential is greater than 1.4 V vs. RHE. The theoretically predicted activation energies of COR R2 and three kinds of WORs are all higher than those experimentally measured at 1.8 V vs. RHE, and it is apparent that these reactions are unlikely to occur. In agreement with experimental results (Fig. 3 *C* and *E* and *SI Appendix*, Fig. S18), none of the possible oxidation products of WORs were detected. Consequently, the carbon anode containing a large quantity of PFRs is unlikely to experience WOR processes when being oxidized.

The effects of different types of N configurations, oxygen functional groups, and carbon defects on COR II on the basis of the initial model were also investigated (*SI Appendix*, Fig. S35). This work did not investigate the effect of S doping on COR II as the organic elemental analysis of the HBC samples showed an S content of 0.00% (*SI Appendix*, Table S11). As illustrated in Fig. 5*D* and *SI Appendix*, Table S12-15, carbon clusters (including various forms of N-doping, oxygen functional groups, and carbon vacancy defects) tend to undergo COR II rather than WORs when carrying unpaired electrons. Furthermore, these structures are more likely to catalyze the oxidation of $OH^-$ to generate *OH, and the RDS for the OER is the transformation of *OOH to $O_2$. The electrocatalytic oxidation process of carbon can be summarized as shown in *SI Appendix*, Fig. S36. Step I, ROIs from water oxidation are successively generated and form covalently bonded oxygen-containing functional groups on carbon anode surface. Step II, further oxidation causes ring-opening of the carbon skeleton and causes the flakes to become increasingly hydrophilic. Until the π–π interactions between the flakes and the carbon layer become weaker and dissolve in the electrolyte.

An energy-saving $H_2$ production system, the SSCA-assisted WE system, was constructed by coupling HER and COR using Pt/C-NF||LHBC-10 electrodes. For comparison, the conventional WE system was also established using Pt/C-NF||$RuO_2$-NF electrodes. The elevation of temperature significantly boosts the activity of SSCA-assisted WE (*SI Appendix*, Fig. S37). As illustrated in Fig. 5*E*, the HER||COR system achieves an industrial-level current density (400 mA $cm^{-2}$) at only 1.24 V at 80 °C, surpassing the performance of a WE system using commercial catalysts. After running the HER||COR system at 50 $mAcm^{-2}_{catalyst}$ for 30 h, the cell voltage only increased to 1.25 V (Fig. 5*F*). The performance of SSCA-assisted WE also outpace recently reported organic compound-assisted WE (*SI Appendix*, Table S16). The Faradaic efficiency for HER is calculated to be >98.8% (Fig. 5*G*) at different current density by collecting the $H_2$ produced. This SSCA-assisted WE could be an effective strategy for energy-saving and secure $H_2$ production.

## Summary

In conclusion, we successfully fabricated a corncob-derived SSCA by a simple hydrothermal reaction and annealing process. The HBC-10 exhibited remarkable electrocatalytic carbon

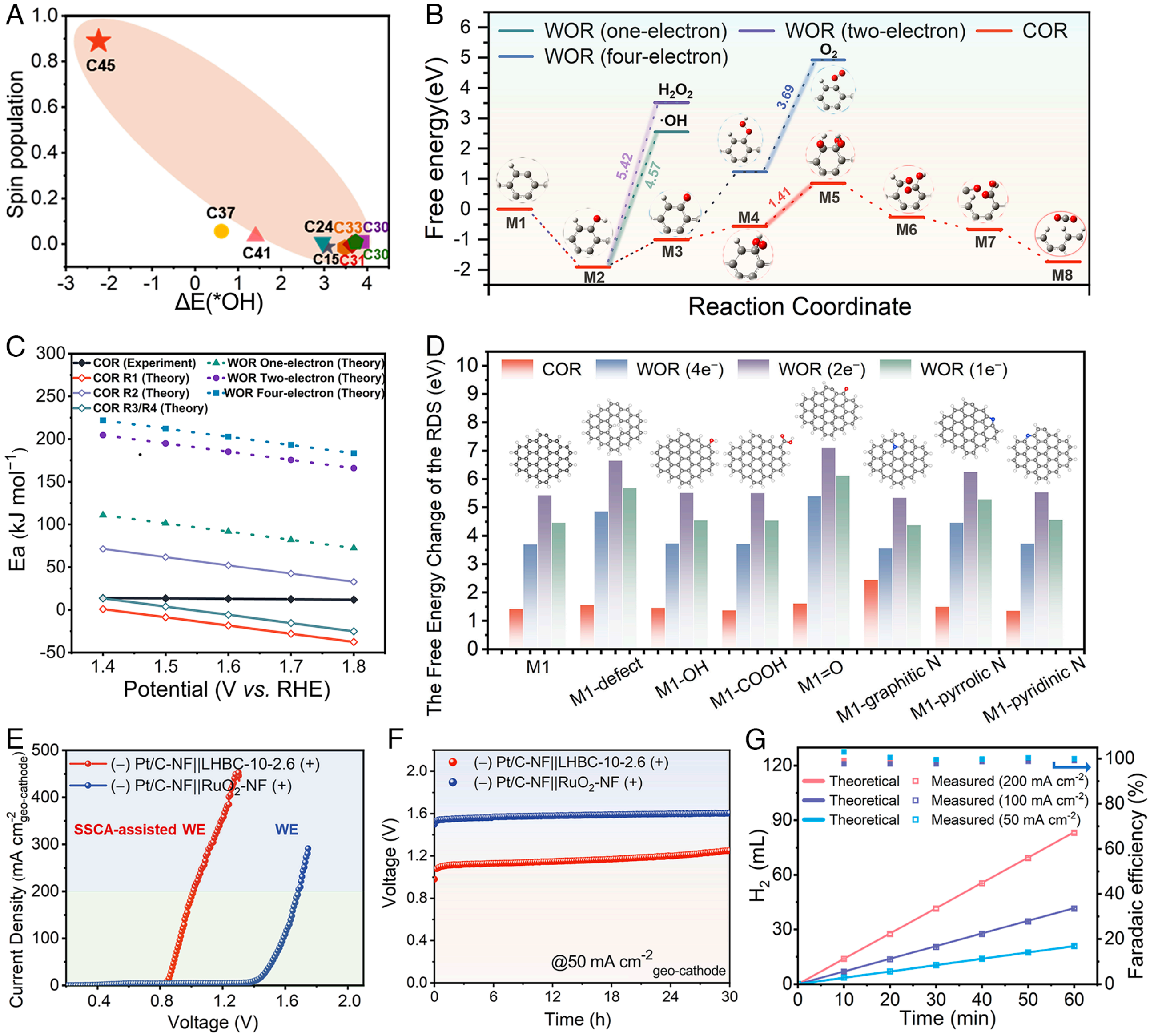

**Fig. 5.** DFT calculations and SSCA-assisted WE performance. (*A*) Different spin population of carbon atoms with versus adsorption energy of *OH; (*B*) the free energy diagrams of COR and WORs for M1, respectively; (*C*) comparison of COR activation energies obtained experimentally with COR and WORs activation energies from theoretical calculations; (*D*) the free energy change of the rate-determining step (RDS) of COR and WORs for carbon clusters with different configurations of N-doped, oxygen functional groups, and carbon vacancy defect, respectively. The carbon, hydrogen, oxygen, and nitrogen elements are represented by gray, white, red, and blue, respectively; (*E*) polarization curves (90%-iR compensation was applied and all currents were normalized to the surface area of the cathode) and (*F*) stability assessment (50 mAcm$^{-2}_{geo-cathode}$) for HER||COR system and HER||OER system at 80 °C, respectively; (*G*) the volume of hydrogen and Faradaic efficiency of HER in SSCA-assisted WE.

oxidation activity due to its abundant unpaired electrons and excellent electron transport capacity. In 1 M KOH electrolyte, the LHBC-10-2.6 drives a high current of 310 mA at an ultralow potential of 1.4 V vs. RHE. The carbon anode could operate at 20 mA for 93 h and the anode potential only increases to 1.4 V vs. RHE. Experiments and DFT calculations have shown that those carbon atoms holding unpaired electrons are the active origin of electrocatalytic oxidation of carbon. Such carbon atoms would promote the oxidation of water molecules (especially one-electron oxidation) and are susceptible to be oxidized by the generated ROIs. Benefiting from the superior COR activity of HBC-10, SSCA-assisted WE system achieves an industrial-level current density of 400 mA cm$^{-2}$ at only 1.24 V at 80 °C, far superior to the conventional WE. This work provides a strategy for low-cost hydrogen production from carbon-based energy conversion.

## Materials and Methods

**Preparation of SSCAs.** Briefly, 5.0 g dried corncobs and 50 mL deionized water were shifted into a 100 mL Teflon-lined stainless steel autoclave and the hydrothermal treatment was held at 200 °C for 24 h. After naturally cooling to room temperature, the samples denoted as HBC were washed with deionized water and then dried in an oven at 80 °C for 6 h. Hydrothermal treatment is the precarbonation of biomass to reduce volatiles and thus increase the carbon yield of biomass after annealing. Next, 0.25 g of HBC sample was filled in a 10 mm diameter mold (*SI Appendix*, Fig. S38). In addition, a 15 MPa pressure was applied to the mold and maintained for 5 min. After demolding, the molded HBC sample was annealed in a tube furnace. Specifically, the HBC samples were calcined at 600 to 1,000 °C for 4 h under $N_2$ atmosphere with a heating rate of 5 °C/min to obtain SSCAs named as HBC-X-Y (X = 6, 7, 8, 9, 10 represents 600 to 1,000 °C, respectively. Y represents the electrode mass in g).

For control experiments and WE experiment, $RuO_2$-NF and Pt/C-NF electrodes were prepared as follows. The electrocatalyst suspensions were obtained by dispersing 2 mg of commercial $RuO_2$ and commercial Pt/C (20 wt%) catalysts in solutions containing 470 μL of ethanol and 30 μL of Nafion, respectively, and sonicating for 30 min. Then, the electrocatalyst suspension was transferred onto nickel foam (1 cm × 1 cm) with a loading of 2 mg $cm^{-2}$.

**Data, Materials, and Software Availability.** All study data are included in the article and/or *SI Appendix*.

**ACKNOWLEDGMENTS.** This work was supported by the National Natural Science Foundation of China (Nos. 52476192 and 52106237) and the Natural Science Foundation of Heilongjiang Province (No. YQ2022E027). We would like to thank Shiyanjia Lab (www.shiyanjia.com) for the support of the transmission electron microscopy test, and Beishide Instrument Technology (Beijing) Co., Ltd. for the pore structure test.

---

Author affiliations: [a]School of Energy Science and Engineering, Harbin Institute of Technology, Harbin 150001, Heilongjiang, People's Republic of China

1. Z. Li *et al.*, Alcohols electrooxidation coupled with $H_2$ production at high current densities promoted by a cooperative catalyst. *Nat. Commun.* **13**, 1–14 (2022).
2. B. Rausch, M. D. Symes, G. Chisholm, L. Cronin, Decoupled catalytic hydrogen evolution from a molecular metal oxide redox mediator in water splitting. *Science* **345**, 1326–1330 (2014).
3. M. W. Kanan, D. G. Nocera, In situ formation of an oxygen-evolving catalyst in neutral water containing phosphate and $Co^{2+}$. *Science* **321**, 1072–1075 (2008).
4. W. F. Xie, M. F. Shao, Alkaline water electrolysis for efficient hydrogen production. *J. Electrochem.* **28**, 22014008 (2022).
5. B. You, Y. Sun, Innovative strategies for electrocatalytic water splitting. *Acc. Chem. Res.* **51**, 1571–1580 (2018).
6. I. Mondal *et al.*, Nanostructured intermetallic nickel silicide (Pre) catalyst for anodic oxygen evolution reaction and selective dehydrogenation of primary amines. *Adv. Energy Mater.* **12**, 2200269 (2022).
7. C. Huang, Y. Huang, C. Liu, Y. Yu, B. Zhang, Integrating hydrogen production with aqueous selective semi-dehydrogenation of tetrahydroisoquinolines over a $Ni_2P$ bifunctional electrode. *Angew. Chem. Int. Ed.* **131**, 12142–12145 (2019).
8. R. Ge *et al.*, Selective electrooxidation of biomass-derived alcohols to aldehydes in a neutral medium: Promoted water dissociation over a nickel-oxide-supported ruthenium single-atom catalyst. *Angew. Chem. Int. Ed.* **61**, e202200211 (2022).
9. Y. Lu *et al.*, Identifying the geometric site dependence of spinel oxides for the electrooxidation of 5-hydroxymethylfurfural. *Angew. Chem. Int. Ed.* **59**, 19215–19221 (2020).
10. K. Jiang *et al.*, Nickel-cobalt nitride nanoneedle supported on nickel foam as an efficient electrocatalyst for hydrogen generation from ammonia electrolysis. *Electrochim. Acta* **403**, 139700 (2022).
11. S. K. Geng *et al.*, Nickel ferrocyanide as a high-performance urea oxidation electrocatalyst. *Nat. Energy* **6**, 904–912 (2021).
12. F. Sun *et al.*, Energy-saving hydrogen production by chlorine-free hybrid seawater splitting coupling hydrazine degradation. *Nat. Commun.* **12**, 1–11 (2021).
13. H. Zhou *et al.*, Electrocatalytic upcycling of polyethylene terephthalate to commodity chemicals and $H_2$ fuel. *Nat. Commun.* **12**, 4679 (2021).
14. H. Zhao *et al.*, Raw biomass electroreforming coupled to green hydrogen generation. *Nat. Commun.* **12**, 1–10 (2021).
15. E. J. Cho, L. T. P. Trinh, Y. Song, Y. G. Lee, H.-J. Bae, Bioconversion of biomass waste into high value chemicals. *Bioresour. Technol.* **298**, 122386 (2020).
16. H. Luo *et al.*, Progress and perspectives in photo-and electrochemical-oxidation of biomass for sustainable chemicals and hydrogen production. *Adv. Energy Mater.* **11**, 2101180 (2021).
17. Z. Fan *et al.*, Recent developments in electrode materials for the selective upgrade of biomass-derived platform molecules into high-value-added chemicals and fuels. *Green Chem.* **24**, 7818–7868 (2022).
18. A. C. Garcia *et al.*, Strong impact of platinum surface structure on primary and secondary alcohol oxidation during electro-oxidation of glycerol. *ACS Catal.* **6**, 4491–4500 (2016).
19. P. Zhang *et al.*, Paired electrocatalytic oxygenation and hydrogenation of organic substrates with water as the oxygen and hydrogen source. *Angew. Chem. Int. Ed.* **131**, 9253–9257 (2019).
20. R. Ge *et al.*, Selective electrooxidation of biomass-derived alcohols to aldehydes in a neutral medium: Promoted water dissociation over a nickel-oxide-supported ruthenium single-atom catalyst. *Angew. Chem. Int. Ed.* **134**, e202200211 (2022).
21. M. T. Bender, X. Yuan, K.-S. Choi, Alcohol oxidation as alternative anode reactions paired with (photo) electrochemical fuel production reactions. *Nat. Commun.* **11**, 4594 (2020).
22. M. S. Houache *et al.*, Electrochemical valorization of glycerol on Ni-rich bimetallic NiPd nanoparticles: Insight into product selectivity using in situ polarization modulation infrared-reflection absorption spectroscopy. *ACS Sustainable Chem. Eng.* **7**, 14425–14434 (2019).
23. J. Li, W. Zhou, Y. Huang, J. Gao, Lignin-assisted water electrolysis for energy-saving hydrogen production with $Ti/PbO_2$ as the anode. *Front. Energy Res.* **9**, 762346 (2021).
24. R. Li *et al.*, Key roles of interfacial $OH^-$ ion distribution on proton coupled electron transfer kinetics toward urea oxidation reaction. *Small* **19**, 2302151 (2023).
25. R. W. Coughlin, M. Farooque, Hydrogen production from coal, water and electrons. *Nature* **279**, 301–303 (1979).
26. Y. Huang *et al.*, Edge and defect sites in porous activated coke enable highly efficient carbon-assisted water electrolysis for energy-saving hydrogen production. *Renewable Energy* **195**, 283–292 (2022).
27. Y. Du, Z. Ying, X. Zheng, B. Dou, G. Cui, Correlating electrochemical biochar oxidation with electrolytes during biochar-assisted water electrolysis for hydrogen production. *Fuel* **339**, 126957 (2023).
28. G. Amikam, N. Fridman-Bishop, Y. Gendel, Biochar-assisted iron-mediated water electrolysis process for hydrogen production. *ACS Omega* **5**, 31908–31917 (2020).
29. W. Zhou *et al.*, Two-step coal-assisted water electrolysis for energy-saving hydrogen production at cell voltage of 1.2 V with current densities larger than 150 $mA/cm^2$. *Energy* **260**, 125145 (2022).
30. Z. Ying *et al.*, Enhancing biochar oxidation reaction with the mediator of $Fe^{2+}/Fe^{3+}$ or $NO^{2-}/NO^{3-}$ for efficient hydrogen production through biochar-assisted water electrolysis. *Energy Convers. Manage.* **244**, 114523 (2021).
31. X. Feng *et al.*, Untangling the respective effects of heteroatom-doped carbon materials in batteries, supercapacitors and the ORR to design high performance materials. *Energy Environ. Sci.* **14**, 2036–2089 (2021).
32. G. Han *et al.*, Tuning edge-oxygenated groups on graphitic carbon materials against corrosion. *Nano Energy* **66**, 104112 (2019).
33. L. Castanheira *et al.*, Carbon corrosion in proton-exchange membrane fuel cells: From model experiments to real-life operation in membrane electrode assemblies. *ACS Catal.* **4**, 2258–2267 (2014).
34. J. Liu *et al.*, Pyrolysis of superfine pulverized coal. Part 4. Evolution of functionalities in chars. *Energy Covers. Manage.* **134**, 32–46 (2017).
35. L. Dong *et al.*, Indian coal pyrolysis behaviour and kinetics study using covalent bond information. *Thermochim. Acta* **711**, 179208 (2022).
36. A. Kumar, A. Ghosh, M. Forsyth, D. R. MacFarlane, S. Mitra, Free-radical catalysis and enhancement of the redox kinetics for room-temperature sodium–sulfur batteries. *ACS Energy Lett.* **5**, 2112–2121 (2020).
37. K. Wang *et al.*, In-situ catalytic conversion of coal pyrolysis gas to nanoporous carbon rods and superior sodium ion storage performance. *Fuel* **281**, 118782 (2020).
38. F. Sun *et al.*, Inexpensive activated coke electrocatalyst for high-efficiency hydrogen peroxide production: Coupling effects of amorphous carbon cluster and oxygen dopant. *Appl. Catal. B, Environ.* **286**, 119860 (2021).
39. F. Sun *et al.*, Carboxyl-dominant oxygen rich carbon for improved sodium ion storage: Synergistic enhancement of adsorption and intercalation mechanisms. *Adv. Energy Mater.* **11**, 2002981 (2021).
40. L. Leng *et al.*, An overview on engineering the surface area and porosity of biochar. *Sci. Total Environ.* **763**, 144204 (2021).
41. X. Ruan *et al.*, Formation, characteristics, and applications of environmentally persistent free radicals in biochars: A review. *Bioresour. Technol.* **281**, 457–468 (2019).
42. J. Zhang *et al.*, Co-monomer control of carbon nitride semiconductors to optimize hydrogen evolution with visible light. *Angew. Chem. Int. Ed.* **51**, 3183–3187 (2012).
43. G. Zhang *et al.*, Iodine modified carbon nitride semiconductors as visible light photocatalysts for hydrogen evolution. *Adv. Mater.* **26**, 805–809 (2014).
44. Y. Ding, Z. A. Qiao, Carbon surface chemistry: New insight into the old story. *Adv. Mater.* **34**, 2206025 (2022).
45. L. R. Radovic, B. Bockrath, On the chemical nature of graphene edges: Origin of stability and potential for magnetism in carbon materials. *J. Am. Chem. Soc.* **127**, 5917–5927 (2005).
46. M. Acik *et al.*, Unusual infrared-absorption mechanism in thermally reduced graphene oxide. *Nat. Mater.* **9**, 840–845 (2010).
47. P. Düngen, R. Schlögl, S. Heumann, Non-linear thermogravimetric mass spectrometry of carbon materials providing direct speciation separation of oxygen functional groups. *Carbon* **130**, 614–622 (2018).
48. Y. Lin *et al.*, Electrocatalytic water oxidation at quinone-on-carbon: A model system study. *J. Am. Chem. Soc.* **140**, 14717–14724 (2018).
49. Y. Song *et al.*, Bifunctional integrated electrode for high-efficient hydrogen production coupled with 5-hydroxymethylfurfural oxidation. *Appl. Catal. B Environ.* **312**, 121400 (2022).
50. Y. Qi *et al.*, Insights into the activity of nickel boride/nickel heterostructures for efficient methanol electrooxidation. *Nat. Commun.* **13**, 1–11 (2022).
51. L. Castanheira *et al.*, Carbon corrosion in proton-exchange membrane fuel cells: From model experiments to real-life operation in membrane electrode assemblies. *ACS Catal.* **4**, 2258–2267 (2014).
52. X. Lu, W. L. Yim, B. H. Suryanto, C. Zhao, Electrocatalytic oxygen evolution at surface-oxidized multiwall carbon nanotubes. *J. Am. Chem. Soc.* **137**, 2901–2907 (2015).
53. S. Möller *et al.*, Online monitoring of electrochemical carbon corrosion in alkaline electrolytes by differential electrochemical mass spectrometry. *Angew. Chem. Int. Ed.* **59**, 1585–1589 (2020).
54. G. Feng *et al.*, Accelerated crystallization of zeolites via hydroxyl free radicals. *Science* **351**, 1188–1191 (2016).
55. M. Rueffer, D. Bejan, N. J. Bunce, Graphite: An active or an inactive anode? *Electrochim. Acta* **56**, 2246–2253 (2011).
56. J. Wei *et al.*, Probing the oxygen reduction reaction intermediates and dynamic active site structures of molecular and pyrolyzed Fe–N–C electrocatalysts by in situ Raman spectroscopy. *ACS Catal.* **12**, 7811–7820 (2022).
57. S. J. Segovia-Sandoval *et al.*, Synthesis and characterization of carbon xerogel/graphene hybrids as adsorbents for metronidazole pharmaceutical removal: Effect of operating parameters. *Sep. Purif. Technol.* **237**, 116341 (2020).
58. S. Y. Lee *et al.*, Synthesis and electrochemical properties of multi-layered SnO/rGO composite as anode materials for sodium ion batteries. *Appl. Surf. Sci.* **612**, 155859 (2022).
59. Y. Liu *et al.*, Self-crosslinking carbon dots loaded ruthenium dots as an efficient and super-stable hydrogen production electrocatalyst at all pH values. *Nano Energy* **65**, 104023 (2019).
60. Y. Zhai *et al.*, Carbon dots as new building blocks for electrochemical energy storage and electrocatalysis. *Adv. Energy Mater.* **12**, 2103426 (2022).